



LAWRENCE
LIVERMORE
NATIONAL
LABORATORY

Mixing at shocked interfaces with known perturbations

C. R. Weber, A. W. Cook, R. Bonazza

August 7, 2012

J. Fluid Mech

Disclaimer

This document was prepared as an account of work sponsored by an agency of the United States government. Neither the United States government nor Lawrence Livermore National Security, LLC, nor any of their employees makes any warranty, expressed or implied, or assumes any legal liability or responsibility for the accuracy, completeness, or usefulness of any information, apparatus, product, or process disclosed, or represents that its use would not infringe privately owned rights. Reference herein to any specific commercial product, process, or service by trade name, trademark, manufacturer, or otherwise does not necessarily constitute or imply its endorsement, recommendation, or favoring by the United States government or Lawrence Livermore National Security, LLC. The views and opinions of authors expressed herein do not necessarily state or reflect those of the United States government or Lawrence Livermore National Security, LLC, and shall not be used for advertising or product endorsement purposes.

Mixing at shocked interfaces with known perturbations

CHRISTOPHER R. WEBER,¹ ANDREW W. COOK²
AND RICCARDO BONAZZA¹

¹University of Wisconsin, Madison, WI 53706, USA

²Lawrence Livermore National Laboratory, Livermore, CA 94551, USA

(Received ?; revised ?; accepted ?. - To be entered by editorial office)

We derive a growth-rate model for the Richtmyer-Meshkov mixing layer, given arbitrary but known initial conditions. The initial growth rate is determined by the net mass flux through the center plane of the perturbed interface immediately after shock passage. The net mass flux is determined by the correlation between the post-shock density and streamwise velocity. The post-shock density field is computed from the known initial perturbations and the shock jump conditions. The streamwise velocity is computed via Biot-Savart integration of the vorticity field. The vorticity deposited by the shock is obtained from the baroclinic torque with an impulsive acceleration. Using the initial growth rate and characteristic perturbation wavelength as scaling factors, the model collapses growth rates over a broad range of Mach numbers, Atwood numbers and perturbation types. The mixing layer at late times exhibits a power-law growth with an average exponent of $\theta = 0.23$.

1. Introduction

An interface separating two fluids of different density can be hydrodynamically unstable when accelerated in the normal direction. The Rayleigh-Taylor instability (RTI) (Rayleigh 1883; Taylor 1950) occurs when the acceleration is constant and directed towards the heavier fluid. The Richtmyer-Meshkov instability (RMI) (Richtmyer 1960; Meshkov 1969) corresponds to impulsive acceleration (e.g., a shock) and results in an unstable interface, regardless of the direction of acceleration. RTI and RMI occur at both very large scales, e.g., astrophysical settings (Aschenbach *et al.* 1995; Jun *et al.* 1996; Hillebrandt & Niemeyer 2000), and very small scales, e.g., inertial confinement fusion (ICF) (Lindl *et al.* 2004). In ICF, microtargets containing D-T fuel are imploded with laser-generated shock waves in facilities such as Omega and the National Ignition Facility. The spherical targets contain surface imperfections, which grow upon shock acceleration. This leads to mixing of the plastic shell with the nuclear fuel, which subsequently reduces yield. RTI and RMI typically both arise in ICF experiments with the domination of one or the other depending on the shape of the laser pulse. An understanding of the various stages of these instabilities is an essential requirement of ICF efforts.

In the case of RMI, the shock deposits baroclinic vorticity on the interface as it traverses the perturbations. For gases of equal adiabatic index, a shock traveling from the light gas to the heavy gas will cause the perturbations to grow; conversely, if the shock travels from heavy to light, the perturbations invert before growing in the opposite direction. If the amplitude of a perturbation (η) is much smaller than its wavelength (λ) then the stability of the interface can be analyzed by linearizing the Euler equations. The solution to the RTI problem can be extended to RMI by assuming an impulsive acceleration. This “impulsive model” describes the growth rate of a sharp, two-dimensional, single-mode

perturbation as $\dot{\eta} = \eta_o A k u_s$, where η_o is the initial amplitude, $A = (\rho_2 - \rho_1)/(\rho_2 + \rho_1)$ is the Atwood number (with ρ_1 and ρ_2 being the densities of the light and heavy fluids, respectively), $k = 2\pi/\lambda$ is the wavenumber and u_s is the speed imparted to the interface by the shock (Richtmyer 1960). Experiments and numerical simulations have shown that the best agreement with the impulsive model is obtained if post-shock, rather than pre-shock, values are used for η_o and A .

For single-mode perturbations with amplitude-to-wavelength ratios greater than about 0.1, nonlinear effects must be considered. For RTI, Layzer (1955) employed the potential flow equations to describe the location and curvature of the tip of the perturbation. Taking this approach for RMI, Hecht *et al.* (1994), Mikaelian (1998) and Goncharov (2002) found an asymptotic perturbation growth rate $\propto 1/t$. Zhang & Sohn (1996), Zhang & Sohn (1997) and Velikovich & Dimonte (1996) found a similar result using a nonlinear perturbation series solution to the incompressible flow equations. Jacobs & Sheeley (1996) and Rikanati *et al.* (1998) modeled the perturbed fluid interface as a series of point vortices. This appears to give a $1/t$ asymptotic growth rate if the point vortices are spaced in a uniform array (Likhachev & Jacobs 2005).

For a multimodal interface, which is more relevant to applications, the evolving interface quickly becomes too convoluted to treat analytically and is typically approximated through model equations. A simple and commonly used approach for both the RMI and RTI is to model the growth of bubbles (light fluid protruding into heavy) and spikes (heavy fluid protruding into light) based on their buoyancy and drag (Alon *et al.* 1995; Dimonte 2000). For RMI, the buoyancy term is zero and the thickness of the mixing layer, h , is assumed to obey the power-law $h = h_0 \tau^\theta$, where τ is a dimensionless time. A different conceptual model treats the mixing layer as an isotropic slab of diffusing turbulence (Barenblatt 1983; Youngs 1994), where the width of the turbulent layer exhibits a power-law with exponent $\theta \leq 2/3$ in the absence of viscous dissipation. These models are only applicable once the layer has developed into a self-similar turbulent state. Most experimental measurements of θ have put it in the range of 0.25-0.5 (Dimonte & Schneider 1997, 2000; Prasad *et al.* 2000). Several experiments have produced linear growth ($\theta = 1$) after reshock (Vetter & Sturtevant 1995; Leinov *et al.* 2009) and likely need a longer observational time to determine the final value of θ , if it exists. There is also evidence that θ depends on the Atwood number and has different values for the bubble and spikes (Dimonte & Schneider 2000). Dependence on the initial conditions has been suggested (Thorner *et al.* 2010) and this remains an open question. It has also been suggested, based on the asymptotic growth of single-mode perturbations, that the interfacial growth rate may be logarithmic (Brouillette 2002).

Many of the reported RMI growth rates lack a proper nondimensionalization, such that the empirical constant of proportionality has (implied) fractional units of time. Dimensional consistency is clearly required for any scaling law to exhibit any degree of universality and finding the proper length and time scales is central to the problem of predicting late-time growth rates. The primary goals of this paper are to (1) introduce the proper length and time scales for nondimensionalizing the RMI growth rate and (2) demonstrate that these parameters can be obtained *a priori*, i.e., from the initial conditions. Our approach is to extend a previous incompressible model (Cotrell & Cook 2007) to the compressible case. We compare the new model to numerical simulations over a broad parameter space and find it to collapse the growth curves quite well. Finally, we fit the collapsed growth curves to an empirical scaling law and report our finding for θ at late times.

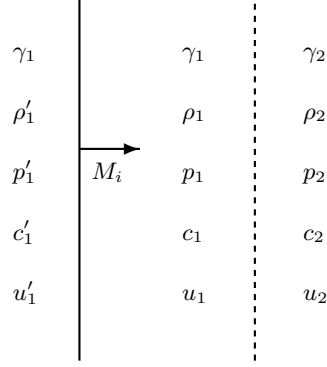


FIGURE 1. A shock of Mach number M_i (solid line) approaching a material discontinuity (dashed line). The coordinate frame is chosen such that the interface is initially located at $x = 0$ and the shock is traveling in the positive x -direction.

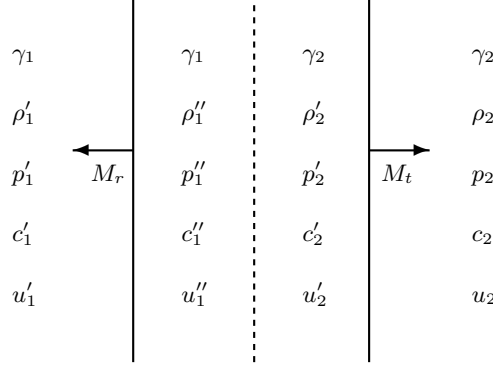


FIGURE 2. After the incident shock in Figure 1 strikes the material interface, a shock of strength M_t is transmitted into fluid 2 and a shock of strength M_r may be reflected back into fluid 1.

2. One-dimensional jump conditions

Consider a shock wave approaching an interface between two different ideal gases, as illustrated in Figure 1. For an interface initially at rest in the lab frame ($u_1 = u_2 = 0$ and $p_1 = p_2$), the state behind the incident shock is:

$$\rho'_1 = \rho_1 \frac{(\gamma_1 + 1)M_i^2}{(\gamma_1 - 1)M_i^2 + 2}, \quad (2.1)$$

$$p'_1 = p_1 \left(\frac{2\gamma_1 M_i^2}{\gamma_1 + 1} - \frac{\gamma_1 - 1}{\gamma_1 + 1} \right), \quad (2.2)$$

$$c'_1 = (\gamma_1 p'_1 / \rho'_1)^{1/2}, \quad (2.3)$$

$$u'_1 = \left(1 - \frac{\rho_1}{\rho'_1} \right) c_1 M_i = \frac{2c_1(M_i^2 - 1)}{(\gamma_1 + 1)M_i} > 0; \quad (2.4)$$

where M_i is the Mach number of the incoming shock and $c_1 = (\gamma_1 p_1 / \rho_1)^{1/2}$. After the shock strikes the interface, a shock of strength M_t is transmitted into fluid 2, while a wave of strength M_r is reflected back into fluid 1. The reflected wave may be either a shock or a rarefaction, as illustrated in Figs. 2 and 3, respectively. After the waves leave the interface, the pressures and velocities across the material discontinuity come back

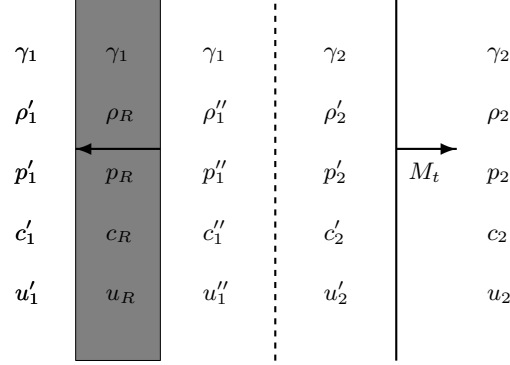


FIGURE 3. After the incident shock in Figure 1 strikes the material interface, a shock of strength M_t is transmitted into fluid 2 and a rarefaction may be reflected back into fluid 1.

into balance; i.e., $u_2' = u_1''$ and $p_2' = p_1''$. The Mach numbers of the incident, transmitted and reflected waves are given by:

$$M_i^2 = \frac{\Pi_i \Lambda_1 + 1}{\Lambda_1 + 1}, \quad \Pi_i \equiv \frac{p_1'}{p_1}, \quad \Lambda_1 \equiv \frac{\gamma_1 + 1}{\gamma_1 - 1}; \quad (2.5)$$

$$M_t^2 = \frac{\Pi_t \Lambda_2 + 1}{\Lambda_2 + 1}, \quad \Pi_t \equiv \frac{p_2'}{p_2}, \quad \Lambda_2 \equiv \frac{\gamma_2 + 1}{\gamma_2 - 1}; \quad (2.6)$$

$$M_r^2 = \frac{\Pi_r \Lambda_1 + 1}{\Lambda_1 + 1}, \quad \Pi_r \equiv \frac{p_1''}{p_1'} = \frac{\Pi_t}{\Pi_i}. \quad (2.7)$$

If $M_r > 1$ then the reflected wave is a shock (Figure 2); whereas, if $M_r < 1$ then the reflected wave is a rarefaction (Figure 3). The velocity behind the transmitted shock is

$$u_2' = \frac{2c_2(M_t^2 - 1)}{(\gamma_2 + 1)M_t} > 0 \quad (2.8)$$

and the velocity behind the reflected wave is

$$u_1'' = u_1' + U_1'' > 0, \quad (2.9)$$

where

$$U_1'' = -\frac{2c_1'(M_r^2 - 1)}{(\gamma_1 + 1)M_r} \quad (2.10)$$

is the velocity behind the reflected wave, measured in the frame moving with u_1' . Matching velocities across the interface yields

$$\frac{2c_2(M_t^2 - 1)}{(\gamma_2 + 1)M_t} = \frac{2c_1(M_i^2 - 1)}{(\gamma_1 + 1)M_i} - \frac{2c_1'(M_r^2 - 1)}{(\gamma_1 + 1)M_r}. \quad (2.11)$$

where $c_2 = (\gamma_2 p_2 / \rho_2)^{1/2}$. Substituting (2.5), (2.6) and (2.7) into (2.11) yields a transcendental equation for Π_t (Wright 1961):

$$\left[\frac{(\Lambda_2 - 1)\rho_1}{(\Lambda_1 - 1)\rho_2} \right]^{1/2} \frac{\Pi_t - 1}{(\Pi_t \Lambda_2 + 1)^{1/2}} = \frac{\Pi_i - 1}{(\Pi_i \Lambda_1 + 1)^{1/2}} - \left(\frac{\rho_1}{\rho_1'} \right)^{1/2} \frac{\Pi_t - \Pi_i}{(\Pi_t \Lambda_1 + \Pi_i)^{1/2}}. \quad (2.12)$$

If $\Pi_t > \Pi_i$ then the reflected wave will be a shock; whereas, if $\Pi_t < \Pi_i$ then the reflected wave will be a rarefaction. Setting $\Pi_t = \Pi_i$ in (2.12) yields the case of no reflection:

$$\frac{\rho_2}{\rho_1} = \frac{(\Pi_i \Lambda_1 + 1)(\Lambda_2 - 1)}{(\Pi_i \Lambda_2 + 1)(\Lambda_1 - 1)} = \frac{\Pi_i(\gamma_1 + 1) + \gamma_1 - 1}{\Pi_i(\gamma_2 + 1) + \gamma_2 - 1} . \quad (2.13)$$

Density ratios larger/smaller than (2.13) will generate reflected shocks/expansions, depending on the strength of the incident shock and the adiabatic indices of the gases. Once (2.12) is solved for Π_t , M_t and M_r can be obtained from (2.6) and (2.7), and the densities behind the transmitted and reflected waves computed as:

$$\rho'_2 = \rho_2 \frac{(\gamma_2 + 1)M_t^2}{(\gamma_2 - 1)M_t^2 + 2} , \quad (2.14)$$

$$\rho''_1 = \rho'_1 \frac{(\gamma_1 + 1)M_r^2}{(\gamma_1 - 1)M_r^2 + 2} . \quad (2.15)$$

All of the preceding equations, including (2.15), are valid regardless of whether the reflected wave is a shock or rarefaction. The incident and transmitted shocks move with lab-frame velocities of $c_1 M_i$ and $c_2 M_t$, respectively. If $M_r > 1$ then the reflected shock moves with a lab-frame velocity of $u'_1 - c'_1 M_r$. If $M_r < 1$ then the reflected rarefaction moves as described in Appendix A.

3. Growth rate of perturbed interface

3.1. Vorticity deposition

A shock crossing a perturbed interface deposits vorticity via baroclinic torque. The vorticity equation for compressible flow is

$$\frac{\partial \boldsymbol{\omega}}{\partial t} + \nabla \times (\boldsymbol{\omega} \times \mathbf{u}) = \frac{1}{\rho^2} \nabla \rho \times \nabla p + \nabla \times \left(\frac{1}{\rho} \nabla \cdot \underline{\boldsymbol{\tau}} \right) , \quad (3.1)$$

where $\underline{\boldsymbol{\tau}}$ is the viscous stress tensor, $\mathbf{u} \equiv (u, v, w)$ is the velocity vector and $\boldsymbol{\omega} \equiv \nabla \times \mathbf{u} = (\omega_x, \omega_y, \omega_z)$ is the vorticity pseudovector. For a thin interface, such that the shock transit time is very short compared to the subsequent evolutionary timescale of the vorticity field, we can model the vorticity deposition as instantaneous and neglect the advective and viscous terms in (3.1); i.e., for an impulsive acceleration

$$\frac{\partial \boldsymbol{\omega}}{\partial t} \approx \frac{1}{\rho^2} \nabla \rho \times \nabla p . \quad (3.2)$$

The pressure gradient in (3.2) satisfies the momentum equation

$$\frac{\partial \rho \mathbf{u}}{\partial t} + \nabla \cdot (\rho \mathbf{u} \mathbf{u}) = -\nabla p + \nabla \cdot \underline{\boldsymbol{\tau}} . \quad (3.3)$$

As a first-order approximation to an impulsive acceleration, we may neglect the viscous and nonlinear terms in (3.3). And by further assuming that the shock remains essentially planar, the pressure gradient becomes:

$$\frac{\partial p}{\partial x} \approx -\frac{\partial \rho u}{\partial t} , \quad (3.4)$$

$$\frac{\partial p}{\partial y} \approx 0 , \quad (3.5)$$

$$\frac{\partial p}{\partial z} \approx 0 . \quad (3.6)$$

Inserting (3.4)-(3.6) into (3.2) yields

$$\frac{\partial \omega_x}{\partial t} \approx 0 , \quad (3.7)$$

$$\frac{\partial \omega_y}{\partial t} \approx -\frac{1}{\rho^2} \frac{\partial \rho}{\partial z} \frac{\partial \rho u}{\partial t} , \quad (3.8)$$

$$\frac{\partial \omega_z}{\partial t} \approx \frac{1}{\rho^2} \frac{\partial \rho}{\partial y} \frac{\partial \rho u}{\partial t} . \quad (3.9)$$

The impulsive approximation allows us to separate the spatial and temporal dependence of ρ and u as follows:

$$\rho \approx \rho^- + (\rho^+ - \rho^-) \mathcal{H}(t) , \quad (3.10)$$

$$u \approx u_s \mathcal{H}(t) ; \quad (3.11)$$

where $\rho^- = \rho(x, y, z, 0^-)$ is the density field just prior to the shock-interface interaction, $\rho^+ = \rho(x, y, z, 0^+)$ is the density just after shock passage, $u_s = u_1' = u_2' > 0$ is the post-shock streamwise velocity of the interface and $\mathcal{H}(t)$ denotes the right-continuous Heaviside function with $\mathcal{H}(0) = 1$, such that $\mathcal{H}^2 = \mathcal{H}$. Thus, according to our impulsive model, we have:

$$\rho^2 = \rho^- \rho^- + (\rho^+ \rho^+ - \rho^- \rho^-) \mathcal{H}(t) , \quad (3.12)$$

$$\frac{\partial \rho}{\partial z} = \frac{\partial \rho^-}{\partial z} + \left(\frac{\partial \rho^+}{\partial z} - \frac{\partial \rho^-}{\partial z} \right) \mathcal{H}(t) , \quad (3.13)$$

$$\frac{\partial \rho}{\partial y} = \frac{\partial \rho^-}{\partial y} + \left(\frac{\partial \rho^+}{\partial y} - \frac{\partial \rho^-}{\partial y} \right) \mathcal{H}(t) , \quad (3.14)$$

$$\frac{\partial \rho u}{\partial t} = \rho^+ u_s \delta(t) . \quad (3.15)$$

Integrating (3.7), (3.8) and (3.9) over the impulse yields:

$$\omega_x^+ \equiv \int_{0^-}^{0^+} \frac{\partial \omega_x}{\partial t} dt \approx 0 , \quad (3.16)$$

$$\omega_y^+ \equiv \int_{0^-}^{0^+} \frac{\partial \omega_y}{\partial t} dt \approx -\frac{u_s}{\rho^+} \frac{\partial \rho^+}{\partial z} , \quad (3.17)$$

$$\omega_z^+ \equiv \int_{0^-}^{0^+} \frac{\partial \omega_z}{\partial t} dt \approx \frac{u_s}{\rho^+} \frac{\partial \rho^+}{\partial y} . \quad (3.18)$$

3.2. Post-shock density and velocity

The initial density field, with a discontinuous interface between the two fluids, can be represented as

$$\rho^-(x, y, z) = \rho_1 + (\rho_2 - \rho_1) H(x - \eta(y, z)) , \quad (3.19)$$

where $\eta(y, z)$ describes the known interfacial perturbations and H is the Heaviside function with $H(0) = 1/2$. (The choice of $H(0) = 1/2$ here leads to simplified expressions involving the Atwood number.) The post-shock density field is given by

$$\rho^+(x, y, z) = \rho_1'' + (\rho_2' - \rho_1'') H(x - \eta^+(y, z)) , \quad (3.20)$$

where $\eta^+(y, z)$ represents the shocked perturbations, which have been compressed and slightly shifted with respect to η . We can write η^+ in terms of η by considering the distance each point on the interface moves during the time it takes for the shock to cross the perturbations. If the interface were flat ($\eta = 0$) then the incident shock would reach every point on η at the same time, in which case η^+ would coincide with η , since no point on the surface would have any time to move relative to any other point. For $\eta \neq 0$ however, the incident shock takes a finite amount of time to cross from the valleys ($\eta < 0$) to the peaks ($\eta > 0$) of the perturbations. During this time, points on the shocked valleys move relative to points on the unshocked peaks. The time it takes for the regions of the shock traveling in gas 1 to pass from $x = \eta < 0$ to $x = 0$ is $t_\eta = -\eta/(M_i c_1)$. (Conversely and equivalently, it takes a time of $t_\eta = \eta/(M_i c_1)$ for the regions of the shock traveling in gas 1 to pass from $x = 0$ to $x = \eta > 0$). During this time, shocked points on the interface travel a distance $u_s t_\eta$ with respect to unshocked points. We will refer to this as the “compression distance”, since it accounts for the reduction in perturbation amplitude, independent of the direction of shock propagation. In addition to the compression effect, which does not move the points at $x = 0$, the shock shifts the entire interface a small amount in the streamwise direction. The time associated with this shift can be thought of as the time it takes the shock to clear the perturbations on the opposite side of the interface. We will refer to the shifting distance simply as x^+ and will show later on that it need not be determined in order to compute the growth of the perturbations. Taking into account both compression and shifting effects, the total distance traveled by each point on the perturbed interface during shock passage is $\eta^+ - \eta = u_s t_\eta + x^+$; hence,

$$\eta^+ = \left(1 - \frac{u_s}{M_i c_1}\right) \eta + x^+ . \quad (3.21)$$

Inserting (3.20) into (3.17) and (3.18) yields:

$$\omega_y^+ \approx \frac{u_s (\rho'_2 - \rho'_1)}{\rho'_1 + (\rho'_2 - \rho'_1)} \frac{\partial \eta^+}{\partial z} \delta(x - \eta^+) , \quad (3.22)$$

$$\omega_z^+ \approx -\frac{u_s (\rho'_2 - \rho'_1)}{\rho'_1 + (\rho'_2 - \rho'_1)} \frac{\partial \eta^+}{\partial y} \delta(x - \eta^+) . \quad (3.23)$$

Once the post-shock vorticity field is obtained, the fluctuating velocity field can be calculated from the Biot-Savart law. If the post-shock velocity fluctuations are small compared to the local speed of sound then the mixing layer evolves in a nearly incompressible fashion and the velocity can be considered divergence free. The Biot-Savart law for a non-divergent flow is

$$\mathbf{u}^+(\mathbf{x}) = \frac{1}{4\pi} \int_{-\infty}^{\infty} \int_{-\infty}^{\infty} \int_{-\infty}^{\infty} \frac{\boldsymbol{\omega}^+(\mathbf{x}^*) \times (\mathbf{x} - \mathbf{x}^*)}{\|\mathbf{x} - \mathbf{x}^*\|^3} dx^* dy^* dz^* , \quad (3.24)$$

where $\mathbf{u}^+ \equiv (u^+, v^+, w^+)$ is the post-shock velocity vector in the frame moving with u_s (and shifted by $-x^+$ with respect to the interface). Inserting (3.16), (3.22) and (3.23) into (3.24) gives:

$$u^+ \approx \frac{u_s A^+}{2\pi} \int_{-\infty}^{\infty} \int_{-\infty}^{\infty} \frac{\frac{\partial \eta^+(y^*, z^*)}{\partial y^*} (y - y^*) + \frac{\partial \eta^+(y^*, z^*)}{\partial z^*} (z - z^*)}{[(x - \eta^+(y^*, z^*))^2 + (y - y^*)^2 + (z - z^*)^2]^{3/2}} dy^* dz^* , \quad (3.25)$$

$$v^+ \approx -\frac{u_s A^+}{2\pi} \int_{-\infty}^{\infty} \int_{-\infty}^{\infty} \frac{\frac{\partial \eta^+(y^*, z^*)}{\partial y^*} (x - \eta^+(y^*, z^*))}{[(x - \eta^+(y^*, z^*))^2 + (y - y^*)^2 + (z - z^*)^2]^{3/2}} dy^* dz^* , \quad (3.26)$$

$$w^+ \approx -\frac{u_s A^+}{2\pi} \int_{-\infty}^{\infty} \int_{-\infty}^{\infty} \frac{\frac{\partial \eta^+(y^*, z^*)}{\partial z^*} (x - \eta^+(y^*, z^*))}{[(x - \eta^+(y^*, z^*))^2 + (y - y^*)^2 + (z - z^*)^2]^{3/2}} dy^* dz^* , \quad (3.27)$$

where

$$A^+ \equiv \frac{\rho'_2 - \rho''_1}{\rho'_2 + \rho''_1} \quad (3.28)$$

is the post-shock Atwood number.

3.3. Interfacial mass flux

Now let $\xi(\mathbf{x}, t)$ denote the mole fraction of gas 2. We quantify the mixed fluid as the mole fraction of chemical product that would be formed from an infinite-rate equimolar reaction between the gases; i.e.,

$$\psi(\xi) \equiv \begin{cases} 2\xi & \text{if } \xi \leq 1/2 \\ 2(1 - \xi) & \text{if } \xi > 1/2 \end{cases} . \quad (3.29)$$

The width of the mixing region is defined as the thickness of mixed fluid that would result if the entrained gases were perfectly homogenized in y and z , i.e.,

$$h(t) \equiv \int_{-\infty}^{\infty} \psi(\langle \xi \rangle) dx , \quad (3.30)$$

where the angle brackets denote a spanwise planar average; i.e.,

$$\langle \xi \rangle(x, t) \equiv \frac{1}{L_y L_z} \int_0^{L_z} \int_0^{L_y} \xi(x, y, z, t) dy dz , \quad (3.31)$$

where L_y and L_z are the spanwise dimensions (height and depth) of the flow domain. If $x = x_s$ is the streamwise location where $\langle \xi \rangle = 1/2$ then for $x \leq x_s$, $\langle \xi \rangle \leq 1/2$; and for $x > x_s$, $\langle \xi \rangle > 1/2$. Differentiating (3.30) with respect to time yields

$$\begin{aligned} \frac{dh}{dt} &= 2 \left\{ \int_{-\infty}^{x_s} \frac{\partial \langle \xi \rangle}{\partial t} dx + \langle \xi \rangle(x_s, t) \frac{dx_s}{dt} - \int_{x_s}^{\infty} \frac{\partial \langle \xi \rangle}{\partial t} dx - \frac{dx_s}{dt} + \langle \xi \rangle(x_s, t) \frac{dx_s}{dt} \right\} \\ &= 2 \left\{ \int_{-\infty}^{x_s} \frac{\partial \langle \xi \rangle}{\partial t} dx - \int_{x_s}^{\infty} \frac{\partial \langle \xi \rangle}{\partial t} dx \right\} , \end{aligned} \quad (3.32)$$

where $dx_s/dt = u_s = \langle u \rangle$ and $\langle \xi \rangle(x_s, t) = 1/2$.

Our assumption that $\nabla \cdot \mathbf{u} \approx 0$ behind the shock implies that mole fractions are nearly equal to volume fractions. We can therefore approximate ξ as

$$\xi \approx \frac{\rho - \rho''_1}{\rho'_2 - \rho''_1} , \quad (3.33)$$

and the average mole fraction as

$$\langle \xi \rangle \approx \frac{\langle \rho \rangle - \rho''_1}{\rho'_2 - \rho''_1} . \quad (3.34)$$

Assuming homogeneity in y and z , the mean continuity equation is

$$\frac{\partial \langle \rho \rangle}{\partial t} = -\frac{\partial \langle \rho u \rangle}{\partial x} = -u_s \frac{\partial \langle \rho \rangle}{\partial x} - \frac{\partial \langle \rho u^* \rangle}{\partial x} , \quad (3.35)$$

where $u^* \equiv u - u_s$ is the streamwise velocity component in the frame moving with the interface. The time derivatives on the right-hand side of (3.32) can thus be written

$$\frac{\partial \langle \xi \rangle}{\partial t} = \frac{1}{\rho'_2 - \rho''_1} \left[-u_s \frac{\partial \langle \rho \rangle}{\partial x} - \frac{\partial \langle \rho u^* \rangle}{\partial x} \right] . \quad (3.36)$$

Inserting (3.36) into (3.32) and using the relations:

$$\langle \rho \rangle (x_s, t) = (\rho_1'' + \rho_2')/2 , \quad (3.37)$$

$$\langle \rho \rangle (-\infty, t) = \rho_1'' , \quad (3.38)$$

$$\langle \rho \rangle (\infty, t) = \rho_2' , \quad (3.39)$$

$$\langle \rho u^* \rangle (-\infty, t) = \langle \rho u^* \rangle (\infty, t) = 0 , \quad (3.40)$$

yields the rate of growth of the mixing region in terms of the net mass flux through the equimolar (x_s) plane; i.e.,

$$\frac{dh}{dt} = \frac{4 \langle \rho u^* \rangle (x_s, t)}{\rho_1'' - \rho_2'} . \quad (3.41)$$

The rate of growth of the mixing region is therefore determined, at all times, solely by the density and fluctuating streamwise velocity on the x_s plane. The initial rate of growth can be estimated *a priori* as

$$\dot{h}^+ \approx \frac{4 \langle \rho^+ u^+ \rangle|_{x^+}}{\rho_1'' - \rho_2'} , \quad (3.42)$$

where ρ^+ is obtained from (3.20), u^+ is obtained from (3.25) and x^+ satisfies

$$\langle \rho^+ \rangle (x^+) = (\rho_1'' + \rho_2')/2 . \quad (3.43)$$

Note that when (3.25) is evaluated at x^+ to compute (3.42), the x^+ in (3.42) cancels the x^+ in (3.21), thus eliminating any dependence of \dot{h}^+ on the shifting distance.

4. Results

4.1. Numerical simulations

The accuracy of (3.42) as well as its efficacy in scaling RMI growth rates are evaluated by comparing the model to the results of statistically converged large-eddy simulations. We solve the compressible Navier-Stokes equations for two fluids using a tenth-order compact differencing scheme combined with a fourth-order Runge-Kutta integrator (Cook 2007, 2009). Energy transfer to subgrid-scales is accomplished through hyperviscosity/hyperdiffusivity models.

Except where otherwise noted, the initial interfacial perturbations, $\eta(y, z)$, are assigned a Gaussian spectrum

$$E_\eta(k) \propto \exp \left(-\frac{(k - k_p)^2}{k_b^2} \right) , \quad (4.1)$$

where $k \equiv \sqrt{k_y^2 + k_z^2}$ is the magnitude of a wavevector in Fourier space, k_p is the peak wavenumber, k_b is the bandwidth, and $E_\eta(k)$ is the two-dimensional energy spectrum of $\eta(y, z)$. The spectrum is computed by taking the two-dimensional (y, z) Fourier transform of $\eta(y, z)$, multiplying by its complex conjugate ($\hat{\eta}^*$), and integrating over circular shells in wavenumber space; i.e.,

$$E(k) \equiv \oint \hat{\eta}^*(k_y, k_z) \hat{\eta}(k_y, k_z) d\sigma , \quad (4.2)$$

where $d\sigma$ is a differential arc-segment in wavenumber space of radius k and

$$\hat{\eta}(k_y, k_z) \equiv \int_{-\infty}^{\infty} \eta(y, z) e^{-i(k_y y + k_z z)} dy dz . \quad (4.3)$$

The net perturbation energy (variance) is given by

$$\eta_{\text{RMS}}^2 = \langle \eta^2 \rangle = \int_0^\infty E_\eta(k) dk . \quad (4.4)$$

The characteristic wavelength of the perturbations is computed as a weighted integral of the spectrum; i.e.,

$$\lambda_0 \equiv 2\pi \frac{\int_0^\infty E(k)/k dk}{\int_0^\infty E(k) dk} . \quad (4.5)$$

The interface is defined by the following error function for the heavy-gas mole fraction

$$\xi(x, y, z) = \frac{1}{2} \left(1 + \text{Erf} \left(\frac{\zeta(x, y, z)}{\sigma} \right) \right) , \quad (4.6)$$

where

$$\zeta(x, y, z) = \text{sign}(x - \eta(\bar{y}, \bar{z})) \min_{\bar{y}, \bar{z}} \left(\sqrt{(x - \eta(\bar{y}, \bar{z}))^2 + (y - \bar{y})^2 + (z - \bar{z})^2} \right) \quad (4.7)$$

is the minimum signed distance to the interface. In the present simulations, σ is set to 2Δ , where Δ is the grid spacing. This ensures numerical stability with a reasonably sharp interface.

The peak and bandwidth of the initial perturbation spectrum must be chosen to ensure that: (a) the initial perturbations are well resolved (their wavelengths are large compared to σ) and (b) the modes have room to grow without influence from the side boundaries. After running a variety of simulations, we determined that setting $\lambda_p = 2\pi/k_p = 32\Delta$ and $k_b = k_p/2$ meets both of these goals. Additionally, we applied a high-pass filter of $\lambda > L_y/4 = 64\Delta$ to ensure that “ambient” low modes don’t unduly influence the late-time self-similar development of the spectrum.

The domain is discretized onto a grid with 512 grid points in the streamwise (x) direction and 256 grid points in each of the spanwise (y and z) directions, with a grid spacing of $\Delta = 0.025$ cm. At this resolution, the interface approximates a discontinuity and the domain contains enough scale separation to allow the spectrum to begin developing an inertial range. To ensure that the growth rates are fully converged, we performed a resolution study in which two lower-resolution simulations were initialized with the same gas properties and perturbations. These other two cases used grid spacings of $\Delta = 0.05$ and 0.1 cm, and contained 128 and 64 points in the spanwise directions, respectively. The profile thickness was kept at $\sigma = 2\Delta$, so the physical thickness increased with decreasing resolution. The full-resolution 256×256 -point perturbation field, $\eta(y, z)$, was subsampled for the lower-resolution simulations. Figure 4(a) shows the growth rate of the mixing layer normalized by (3.42). At lower resolutions, the initial equimolar plane contains larger percentages of mixed fluid (due to the larger value of σ), which reduces the initial growth rate. At a resolution of $N_y = 256$, the peak growth rate is within 3% of \dot{h}^+ , signifying that the initial conditions are sufficiently well resolved to approximate a discontinuous interface. Beyond $t\dot{h}^+/\lambda_0 > 2$ there is little noticeable difference in the growth rates between the simulations at $N_y = 128$ and $N_y = 256$. The energy spectrum of the streamwise component of velocity, u , is shown in Figure 4(b) at $t\dot{h}^+/\lambda_0 = 30$. At the highest resolution, an inertial range of $k^{-5/3}$ appears to form at large wavenumbers.

The speed of the reference frame of the domain is set to $u = -u_s$, so that the post-shock interface is nearly stationary. The incident shock wave and the interface are set to coincide at the center of the domain. The unshocked conditions are set to atmospheric pressure and a temperature of 293 K. The spanwise boundaries in the y - and z -directions are periodic, while the boundaries in the streamwise (x) direction are non-reflecting

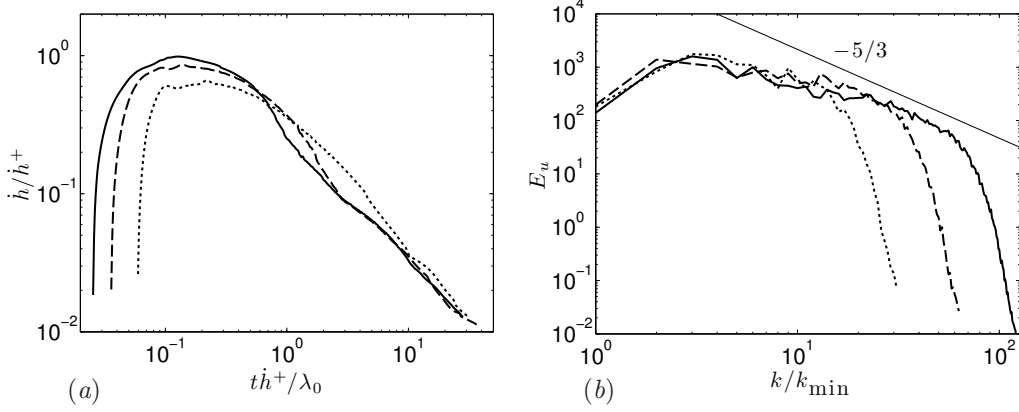


FIGURE 4. (a) Scaled mixing-layer growth rate and (b) streamwise energy spectra at $t h^+ / \lambda_0 = 30$ from simulations using three different resolutions: \cdots , $N_x/2 = N_y = N_z = 64$, $\Delta = 0.1$ cm; $---$, $N_x/2 = N_y = N_z = 128$, $\Delta = 0.05$ cm.; $—$, $N_x/2 = N_y = N_z = 256$, $\Delta = 0.025$ cm. The Mach and Atwood numbers are $M_i = 1.5$ and $A = 0.53$. A fiducial corresponding to $k^{-5/3}$ is drawn in (b) for reference.

case #	gas 1	gas 2	A	M_i	$\eta_{\text{RMS}}/\lambda_0$	$\eta_{\text{RMS}}^+/\lambda_0$
1	Ar	Kr	0.35	1.5	0.1	0.067
2-4	Ar	Xe	0.53	1.5	0.1	0.059
5	Ne	Xe	0.73	1.5	0.1	0.076
6	Ar	Xe	0.53	1.1	0.1	0.091
7	Ar	Xe	0.53	1.9	0.1	0.060
8	Ar	Xe	0.53	1.5	0.05	0.034
9	Ar	Xe	0.53	1.5	0.2	0.134
10	Ar	Xe	0.53	1.5	0.4	0.280
11	Kr	Ar	-0.35	1.5	0.1	0.051
12	Xe	Ar	-0.53	1.5	0.1	0.046
13	Xe	Ne	-0.73	1.5	0.1	0.040
14	Xe	Ar	-0.53	1.1	0.1	0.083
15	Xe	Ar	-0.53	1.9	0.1	0.030
16	Xe	Ar	-0.53	1.5	0.05	0.023
17	Xe	Ar	-0.53	1.5	0.2	0.092

TABLE 1. Simulation parameters. Each case uses $N_x = 512$, $N_y = N_z = 256$, $\Delta = 0.025$ cm, $\lambda_p/\Delta = 32$.

(Poinsot & Lele 1992). To further eliminate spurious reflections, the transmitted and reflected shock waves are directly removed once they near the x -boundaries.

The gas pairs, Mach numbers, and ratios of rms-amplitude to dominant wavelength used in this work are reported in Table 1. Also reported is the ratio of compressed amplitude to dominant wavelength, based on (3.21). The initial perturbations in all cases, except 3 and 4, fit a Gaussian spectrum. Cases 3 and 4 will be discussed at the end of Sec. (4.3.1).

4.2. Modeled mass flux compared to simulations

The efficacy of (3.42) for scaling RMI growth rates depends on the accuracy of (3.20) and (3.25) for predicting the post-shock mass flux through the equimolar plane. Figure 5

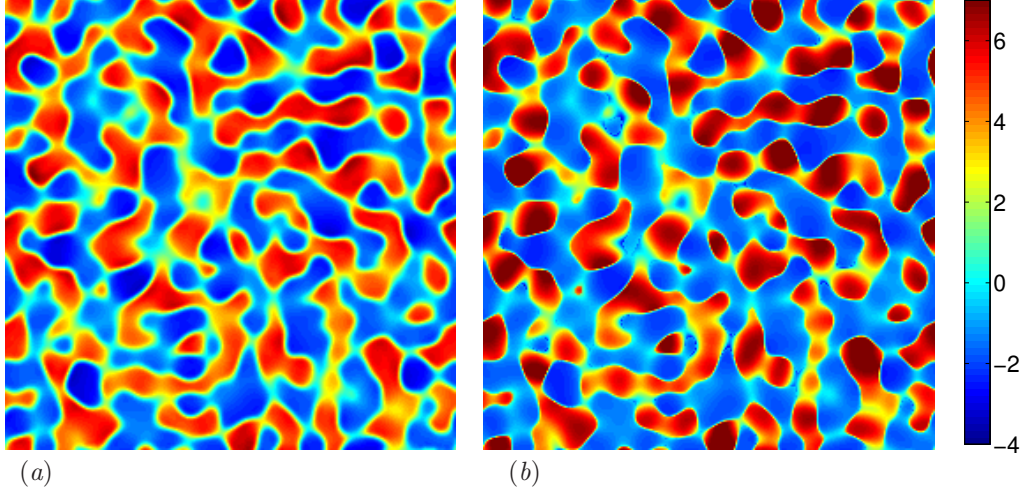


FIGURE 5. Mass flux through the equimolar plane from the (a) case-6 simulation (ρu^*) and (b) model ($\rho^+ u^+$). Units are $\text{g}/(\text{cm}^2 \cdot \text{s})$.

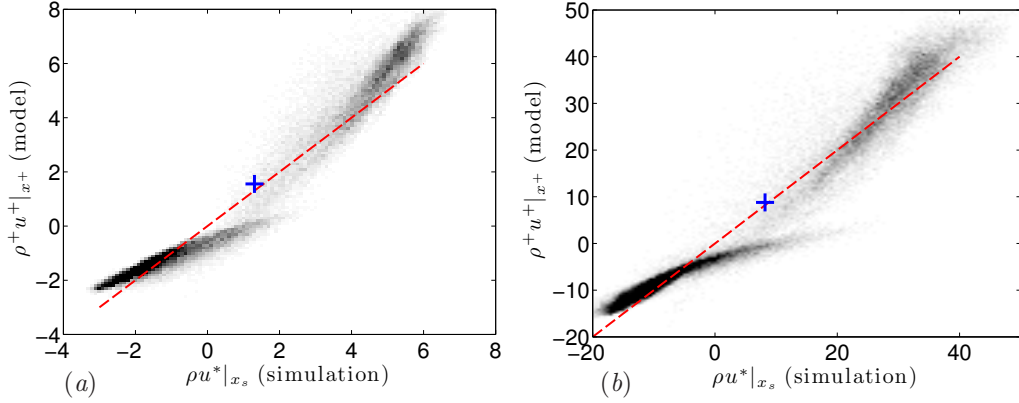


FIGURE 6. Scatter plots of mass flux through the equimolar plane between the model and simulation for an $A = 0.53$ and $\eta_{\text{RMS}}/\lambda_0 = 0.1$ case with Mach number (a) $M=1.1$ and (b) $M_i = 1.5$. Perfect correlation between the model and simulation is shown as a red dashed line. The mean value of mass flux is shown as a blue cross. Units are $\text{g}/(\text{cm}^2 \cdot \text{s})$.

shows ρu^* on the equimolar plane, shortly after shock passage in the case-6 simulation, compared to $\rho^+ u^+$ from the model. The simulation data are extracted immediately after the shock wave has passed completely through the $x = x_s = x^+$ plane. The two images show strong agreement between the model and the simulation, with small differences at high mass-flux values. These minor differences are due to the planar approximation for the shock, the impulsive assumption (zero transit time) and the finite (diffusive) thickness of the initial interface. Fortunately, the model errors tend to cancel out when the average is taken in the spanwise directions.

The cross correlation between ρu^* and $\rho^+ u^+$ is shown in Figure 6 for two different Mach numbers. The local values of the mass flux are in reasonable agreement between the model and the simulations. More importantly however, the average values (which is all that matters in terms of the modeling) of the model are close to the average values of the simulations (as indicated by the proximity of the blue crosses to the red dashed

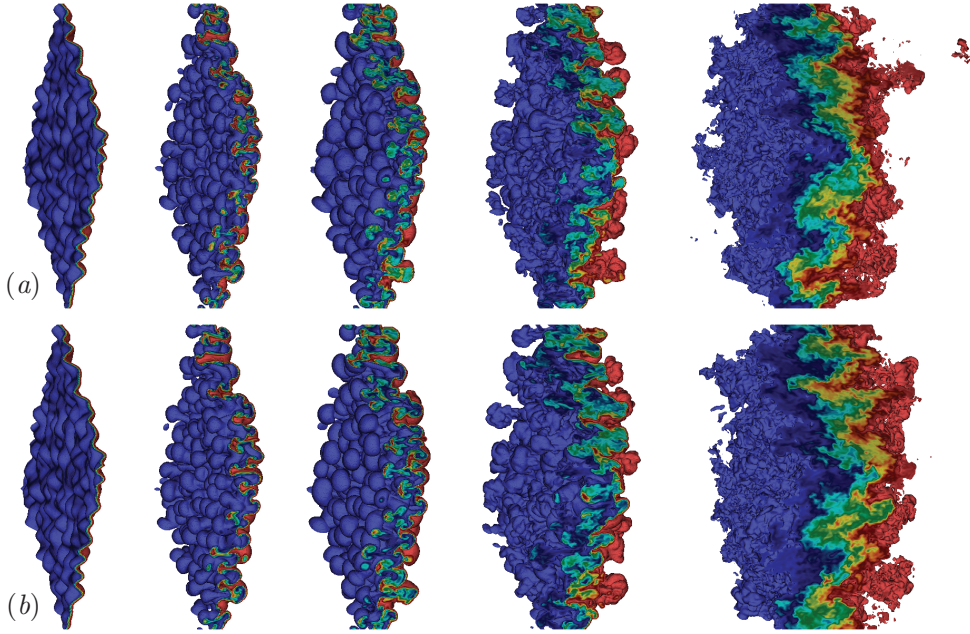


FIGURE 7. Mixed fluid ($0.05 < \xi < 0.95$) at (from left to right) $t\dot{h}^+/\lambda_0 = 0, 1, 2, 5$, and 30 . Initial Mach and Atwood numbers are (a) $M_i = 1.5$ and $A = 0.35$ and (b) $M_i = 1.1$ and $A = 0.53$.

lines). For the $M=1.1$ case, the model mean is larger than the simulation by 20%. For the $M_i = 1.5$ case, the mean mass flux from the model is 9% larger than that of the simulation.

4.3. Scaling the growth rate

With \dot{h}^+ and λ_0 computable from the initial conditions, we wish to assess the universality of the functional form

$$\frac{\dot{h}}{\dot{h}^+} \approx f\left(\frac{t\dot{h}^+}{\lambda_0}\right) \quad (4.8)$$

for modeling RMI growth rates. To illustrate the value of \dot{h}^+ and λ_0 as scaling parameters, images of the mixing layer from two different simulations are compared at the same dimensionless times in Figure 7. Despite the difference in Mach numbers and Atwood numbers, the mixing layer is visually similar at the same nondimensional times. At the first three times indicated ($t\dot{h}^+/\lambda_0 = 0, 1$, and 2), the perturbations grow essentially independently, without significant interaction between neighboring perturbations or secondary instability growth. By $t\dot{h}^+/\lambda_0 = 5$, smaller scale features are developing within the mixing region. By the latest time ($t\dot{h}^+/\lambda_0 = 30$), the layer appears to be weakly turbulent, with an increased amount of mixed fluid in its interior.

4.3.1. Light-to-heavy cases

We performed a series of simulations in which the shock travels from the light gas to the heavy gas, generating a reflected shock at the interface. Figure 8 shows growth rates of the mixing region from simulations using three different Atwood numbers: $A = 0.35$, $A = 0.53$, and $A = 0.73$. The dimensional growth rates are shown on a log-log scale in

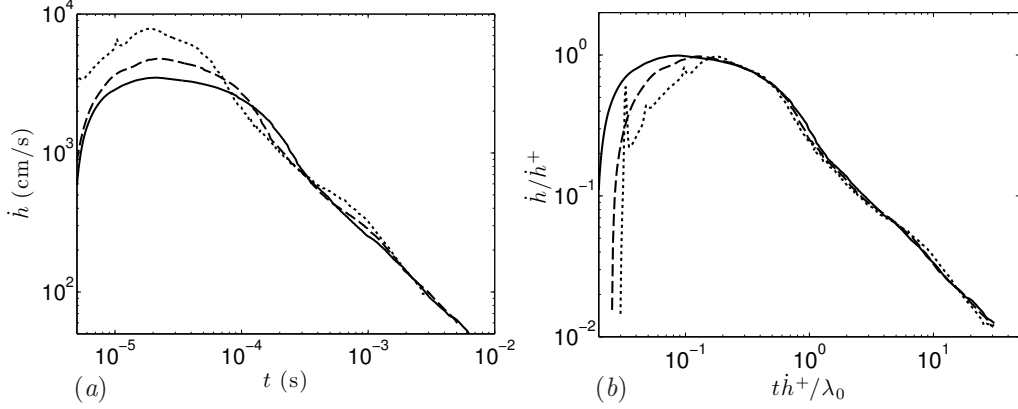


FIGURE 8. Unscaled and scaled mixing-layer growth rate with three different Atwood numbers: —, $A = 0.35$; ----, $A = 0.53$; ·····, $A = 0.73$. The Mach number is $M_i = 1.5$ and the ratio of perturbation amplitude to dominant wavelength is $\eta_{\text{RMS}}/\lambda_0 = 0.1$.

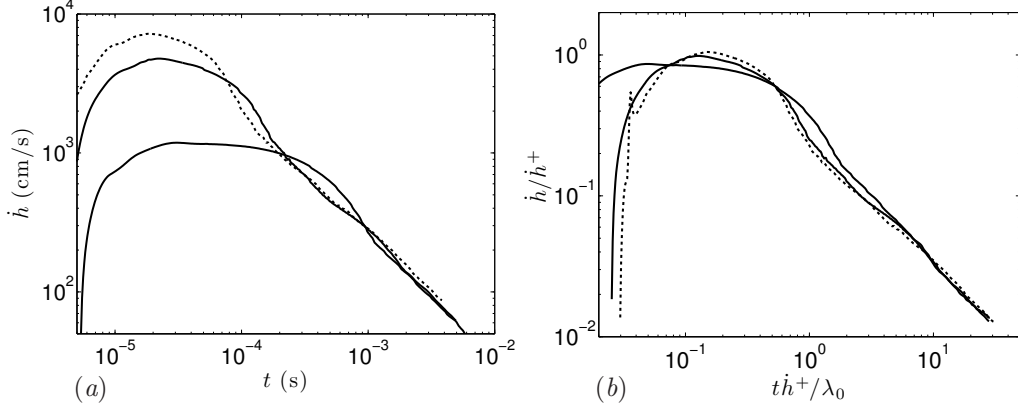


FIGURE 9. Unscaled and scaled mixing-layer growth rate with three different Mach numbers: —, $M_i = 1.1$; ----, $M_i = 1.5$; ·····, $M_i = 1.9$. The Atwood number is $A = 0.53$ and the ratio of perturbation amplitude to dominant wavelength is $\eta_{\text{RMS}}/\lambda_0 = 0.1$.

Figure 8(a), while the scaled growth rates are shown in Figure 8(b). The peak dimensional growth rates differ by a factor of 2.3, but each peak falls within 1-3% of \dot{h}^+ . The scaled curves collapse after peak growth, with 14% variation at $t\dot{h}^+/\lambda_0 = 10$. The early rise in the growth rate corresponds to the transient signature of the shock traversing the interface. The growth rates are not expected to collapse at very early time because the model applies only after the transmitted and reflected waves have left the interface.

Figure 9 shows growth rates from three cases with shock Mach numbers of $M_i = 1.1$, $M_i = 1.5$, and $M_i = 1.9$. The unscaled peak growth rates for the largest and smallest Mach numbers differ by a factor of 6.1. The growth-rate peak for the two larger Mach numbers are both within 5% of \dot{h}^+ , while the $M_i = 1.1$ case peaks at $\dot{h}/\dot{h}^+ = 0.86$. At $t\dot{h}^+/\lambda_0 = 10$ the three dimensionless growth rates are within 7% of each other.

Figure 10 shows the unscaled and scaled growth rates from four cases using different ratios of rms-amplitude to wavelength; i.e.: $\eta_{\text{RMS}}/\lambda_0 = 0.05, 0.1, 0.2$, and 0.4 . The unscaled peak growth rates differ by a factor of 3.7. The growth-rate peaks for the two smaller amplitude-to-wavelength ratios are both within 3% of \dot{h}^+ , while the $\eta_{\text{RMS}}/\lambda_0 = 0.2$ case

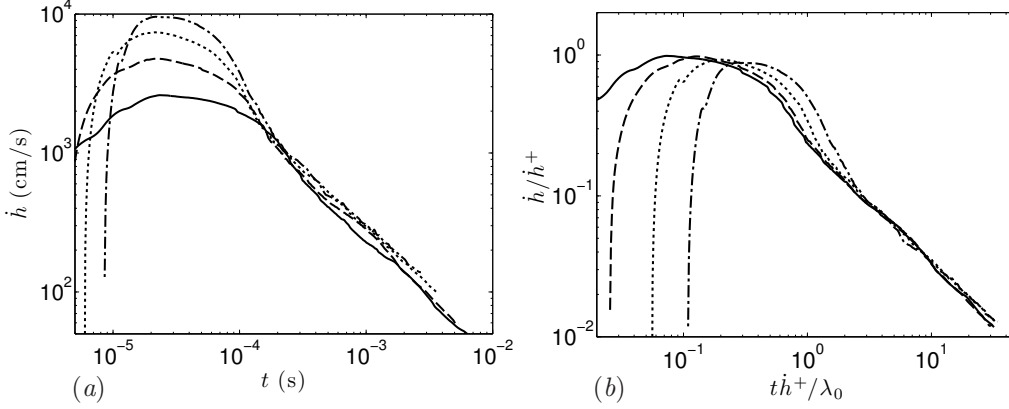


FIGURE 10. Unscaled and scaled mixing-layer growth rate with four different ratios of perturbation amplitude to dominant wavelength: —, $\eta_{\text{RMS}}/\lambda_0 = 0.05$; ----, $\eta_{\text{RMS}}/\lambda_0 = 0.1$; ·····, $\eta_{\text{RMS}}/\lambda_0 = 0.2$; - · - · - , $\eta_{\text{RMS}}/\lambda_0 = 0.4$. The Atwood number is $A = 0.53$ and the Mach number is $M_i = 1.5$.

peaks at $\dot{h}/\dot{h}^+ = 0.93$ and the $\eta_{\text{RMS}}/\lambda_0 = 0.4$ case peaks at $\dot{h}/\dot{h}^+ = 0.88$. As the amplitude increases with respect to the wavelength, the shock becomes increasingly distorted during its traversal of the perturbations, sending refracted waves in the spanwise directions. Additionally, the shock takes a greater amount of time to pass through the perturbed interface. The model, as currently constituted, does not account for these nonideal effects; hence, it's not surprising that it doesn't perform quite as well for large-amplitude perturbations. For initially non-linear perturbations ($\eta_{\text{RMS}}^+/\lambda_0 > 0.1$), the model slightly over-predicts the initial growth rate and the curves do not collapse quite as well at early times. However, beyond $th^+/\lambda_0 > 3$, the growth rates from all four cases collapse, with 8% variation at $th^+/\lambda_0 = 10$.

To examine the model's robustness for different perturbation spectra, three simulations were performed with different initial spectra but with the same flow parameters: $M_i = 1.5$, $A = 0.53$, and $\eta_{\text{RMS}}/\lambda_0 = 0.1$. The initial spectra are shown in Figure 11(a), one of which is the Gaussian spectrum used in the other simulations. The other two spectra are a k^{-2} power-law, which approximates the roughness of an ICF target (Barnes *et al.* 2002), and a bimodal spectrum with peaks at $\lambda = 24\Delta$ and $\lambda = 48\Delta$, which serves to test the efficacy of (4.5) for λ_0 as a scaling parameter. For broadband perturbations, the k^{-2} spectrum has been shown to produce growth with an exponent of $\theta = 2/3$, due to linear-regime growth of unsaturated modes, but a spectral width of several decades is necessary to observe this (Thornber *et al.* 2010). For the cases herein, the spectra are all relatively narrow band, since their widths span less than a decade. The unscaled growth rates resulting from the three different initial spectra are shown in Figure 11(b), where they are seen to differ by only 10%. The scaled growth rates are displayed in 11(c), where all three peak growth rates fall within 3% of \dot{h}^+ . The growth-rates at later times differ between the three cases, with 40% variation in the dimensionless growth rate at $th^+/\lambda_0 = 10$. This behavior is investigated further in Sec. (4.4).

4.3.2. Heavy-to-light cases

In addition to the light-to-heavy cases, we ran a series of simulations in which the shock passed from the heavy gas to the light gas, generating a reflected rarefaction at the interface. These cases differ in that the vorticity deposition induces an initially negative growth rate; i.e., the perturbations decrease in amplitude, invert phase, and then

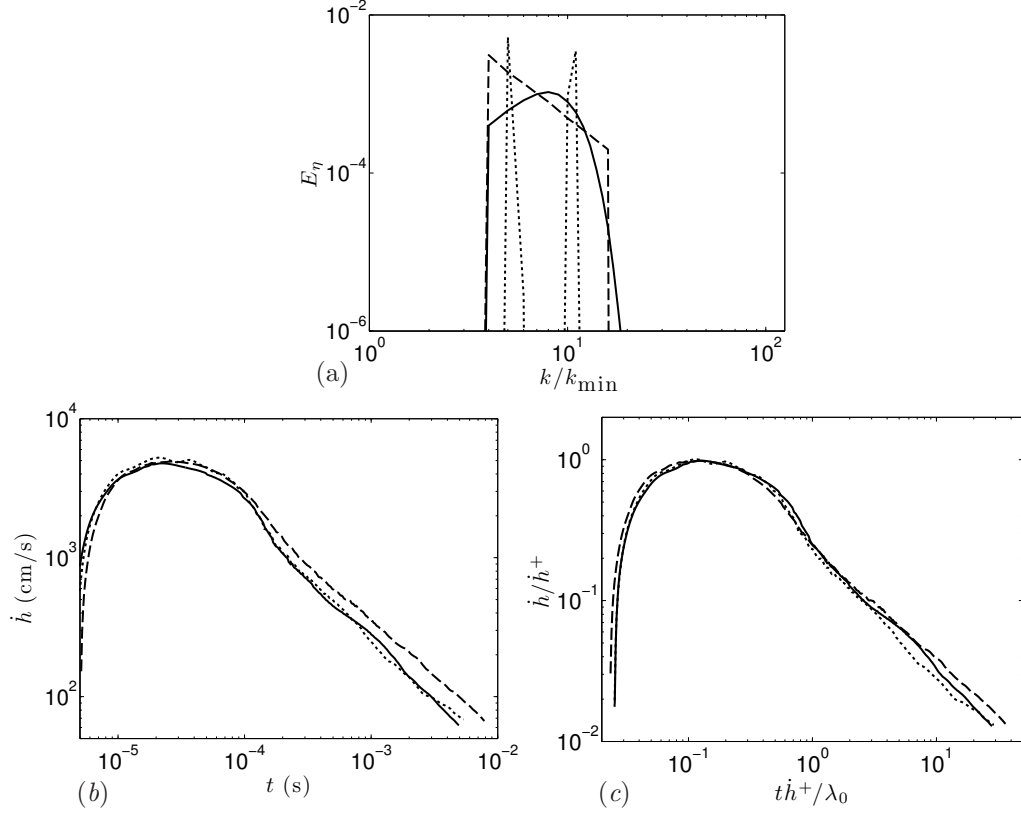


FIGURE 11. Unscaled and scaled mixing-layer growth rate with three different perturbation spectra: —, Gaussian; ----, k^{-2} power-law; ·····, bimodal. The perturbation energy spectra are shown in (a) and the growth rates are shown in (b) and (c). The Atwood numbers is $A = 0.53$, the Mach number is $M_i = 1.5$, and the ratio of perturbation amplitude to dominant wavelength is $\eta_{\text{RMS}}/\lambda_0 = 0.1$.

grow in the opposite direction. For these cases it is necessary to account for the phase-inversion time; i.e., to begin comparison at the time when the mixing-layer thickness reaches its minimum and the growth rate turns positive. The thickness at early time is approximately

$$h(t) = \dot{h}^+ t + h_0^+, \quad (4.9)$$

where \dot{h}^+ is negative for heavy-to-light cases and h_0^+ is the thickness due to shock compression. In practice, h_0^+ is computed from (3.21) and (3.30). The thickness reaches its minimum at an “inversion time” of $t_i = -h_0^+/\dot{h}^+$. In the scaled heavy-to-light plots to follow, we account for this inversion time by shifting the time axis. Since the time scale is based on \dot{h}^+ , the functional form of the scaled growth rate becomes

$$\frac{\dot{h}}{|\dot{h}^+|} \approx f\left(\frac{(t - t_i)|\dot{h}^+|}{\lambda_0}\right) = f\left(\frac{t|\dot{h}^+|}{\lambda_0} - \frac{h_0^+}{\lambda_0}\right). \quad (4.10)$$

The dimensionless inversion time is proportional to the post-shock amplitude-to-wavelength ratio.

In Figure 12, the unscaled and scaled growth rates are shown from three cases where the Atwood number is varied, keeping the other parameters fixed. The peak growth rates

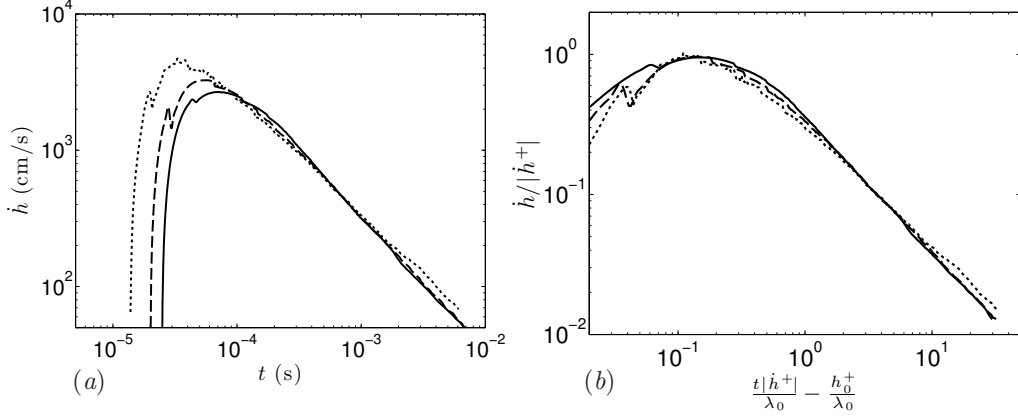


FIGURE 12. (a) Unscaled and (b) scaled mixing-layer growth rate with three different Atwood numbers: —, $A = -0.35$; ----, $A = -0.53$; ·····, $A = -0.73$. The Mach number is $M_i = 1.5$ and the ratio of perturbation amplitude to dominant wavelength is $\eta_{\text{RMS}}/\lambda_0 = 0.1$.

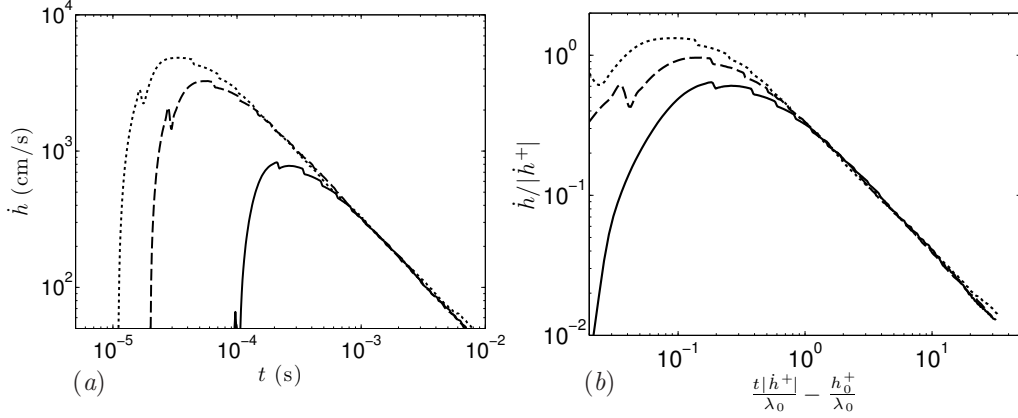


FIGURE 13. Unscaled and scaled mixing-layer growth rate with three different Mach numbers: —, $M_i = 1.1$; ----, $M_i = 1.5$; ·····, $M_i = 1.9$. The Atwood number is $A = -0.53$ and the ratio of perturbation amplitude to dominant wavelength is $\eta_{\text{RMS}}/\lambda_0 = 0.1$.

all fall within 7% of $|\dot{h}^+|$ and the curves collapse well at late time, with 13% variation at a dimensionless time of 10. By accounting for the inversion time, the peaks are brought together in dimensionless time.

Figure 13 shows the growth rates from three cases using Mach numbers $M_i = 1.1$, $M_i = 1.5$ and $M_i = 1.9$. The scaled growth rates exhibit much better collapse than the unscaled growth rates and the peaks are brought nearly in line. However, the higher Mach-number cases still reach higher dimensionless growth rates, which may be partly due to the difference in phase inversion time between the three cases. As the Mach number increases, the dimensionless inversion time, h_0^+/λ_0 , decreases due to shock compression. The three scaled growth-rate curves collapse after a dimensionless time of 1, with only 5% variation at a dimensionless time of 10.

Figure 14 shows the growth rates from three cases using ratios of pre-shock amplitude to wavelength of $\eta_{\text{RMS}}/\lambda_0 = 0.05$, $\eta_{\text{RMS}}/\lambda_0 = 0.1$, and $\eta_{\text{RMS}}/\lambda_0 = 0.2$. Once again, the model is reasonably effective at collapsing the curves. In the scaled plot, the case with the smallest amplitude-to-wavelength ratio reaches the largest peak growth rate. As in

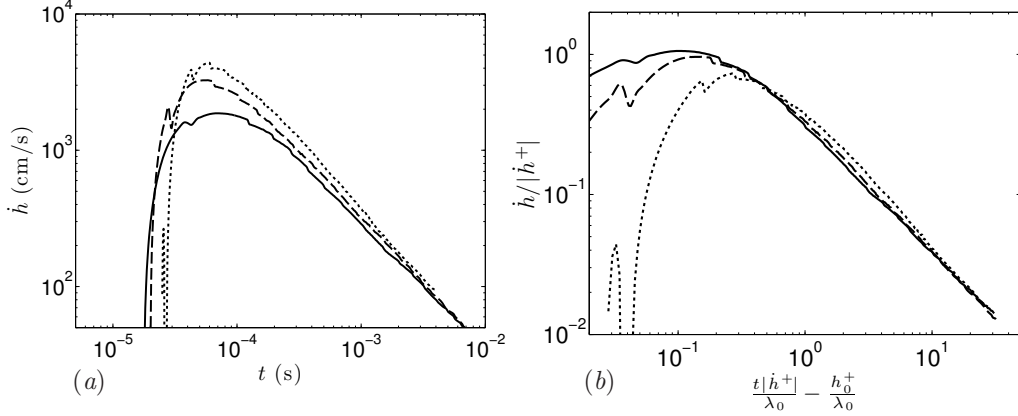


FIGURE 14. Unscaled and scaled mixing-layer growth rate with three different ratios of perturbation amplitude to dominant wavelength: —, $\eta_{\text{RMS}}/\lambda_0 = 0.05$; ----, $\eta_{\text{RMS}}/\lambda_0 = 0.1$; ·····, $\eta_{\text{RMS}}/\lambda_0 = 0.2$. The Atwood numbers is $A = -0.53$ and the Mach number is $M_i = 1.5$.

the previous case, this appears to be related to the difference in phase inversion time. After a dimensionless time of 0.5, the scaled growth rates collapse very well, with 6% variation at a dimensionless time of 10.

4.4. Curve fit to late time growth

The successful collapse of growth rates based on parameters computed *a priori* suggests that a general curve fit can be obtained for the data in Figs. 8-14. We have investigated the following three functional forms:

$$\frac{h - h_{\tau=0}}{\lambda_0} = a\tau^\theta, \quad \frac{\dot{h}}{|\dot{h}^+|} = a\theta\tau^{\theta-1}, \quad (4.11)$$

$$\frac{h - h_{\tau=0}}{\lambda_0} = \frac{(b\tau + 1)^\theta}{b\theta}, \quad \frac{\dot{h}}{|\dot{h}^+|} = (b\tau + 1)^{\theta-1}, \quad (4.12)$$

and

$$\frac{h - h_{\tau=0}}{\lambda_0} = c \ln(d\tau + 1), \quad \frac{\dot{h}}{|\dot{h}^+|} = \frac{cd}{d\tau + 1}, \quad (4.13)$$

where the dimensionless time is

$$\tau = \begin{cases} \frac{t\dot{h}^+}{\lambda_0} & A > 0 \\ \frac{t|\dot{h}^+|}{\lambda_0} + \frac{h_0^+}{\lambda_0} & A < 0 \end{cases}. \quad (4.14)$$

In these equations, $h_{\tau=0}$ is the interface thickness at $\tau = 0$, which is h_0^+ for the light-to-heavy ($A > 0$) cases and zero for the heavy-to-light ($A < 0$) cases. The first two of these equations represents the power-law behavior that results from the buoyancy-drag model and the model of a diffusing/dissipating slab of turbulence. The growth-rate plots of Figs. 8-14 show that the early time behaves differently from the apparent power-law growth rate at later times. Therefore it is not likely that a single model will describe both the early and late-time growth-rate behaviors. For this reason (4.11) and (4.12) contain two fit parameters and each equation only satisfies one of the two boundary conditions of $h(\tau = 0) = h_{\tau=0}$ or $\dot{h}(\tau = 0) = |\dot{h}^+|$. One of these parameters, θ , adjusts the slope

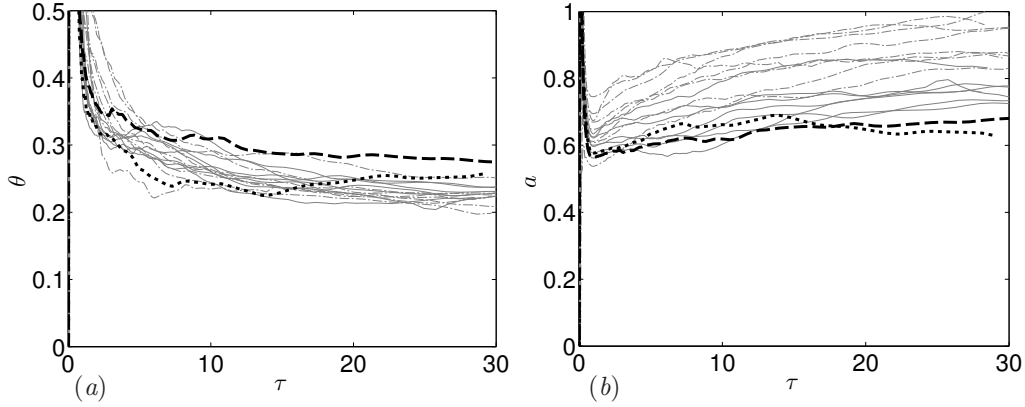


FIGURE 15. Growth rate parameters (a) θ and (b) a , computed using (4.15) from all of the cases in Table 1. Perturbation energy spectra are shown as: — (gray), Gaussian ($A > 0$); - - - - (gray), Gaussian ($A < 0$); - - - -, k^{-2} power-law; ·····, bimodal.

of the layer-thickness or growth-rate curve, while the other, a or b , shifts the magnitude to match the observed simulation data. The third equation, (4.13), is used to test if the mixing-layer behavior is similar to that of a single-mode perturbation, which grows logarithmically at late times.

From (4.11), the dimensionless parameters θ and a can be computed in terms of mixing-layer thickness, growth rate, and dominant wavelength,

$$\theta = \frac{\dot{h}}{|\dot{h}^+|} \frac{\lambda_0}{h - h_{\tau=0}} \tau, \quad a = \frac{h - h_{\tau=0}}{\lambda_0} \tau - \frac{\dot{h}}{|\dot{h}^+|} \frac{\lambda_0}{h - h_{\tau=0}} \tau. \quad (4.15)$$

These parameters are plotted in Figure 15 for all of the simulation data. The exponent θ is decreasing in time, but appears to asymptote to a final value between 0.20 and 0.25 for all of the simulation cases with a Gaussian perturbation spectrum. There does not appear to be any systematic difference in the value of θ between the $A > 0$ and the $A < 0$ cases. The power-law and bimodal perturbations have the largest values of θ , with an average of 0.28 and 0.25, respectively, beyond $\tau > 20$. The coefficient a varies over a wider range, with a final value between 0.6 and 1.0. The larger values of a generally correspond to $A < 0$ cases. An average of all of the data beyond $\tau > 20$ gives $\theta = 0.232$ and $a = 0.815$. The parameters from (4.12) were determined using a least squares method to the mixing-layer thickness data beyond $\tau > 20$ and give $\theta = 0.233$ and $b = 8.97$.

Figure 16 shows the growth rate and the mixing-layer thickness from all of the simulation data along with (4.11) as a red dashed line, (4.12) as a green dot-dashed line, and (4.13) as a blue dotted line. The power-laws use the mean values discussed in the last paragraph. The logarithmic equation was fit using a least squares method to the data beyond $\tau > 20$, which finds $c = 0.404$, and $d = 2.95$. In the growth-rate plot, Figure 16(a), the two power-law equations appear to only fit the late-time data. This is what one would expect given Figure 15(a), where the apparent value of θ is larger at earlier times. The power-law growth does appear to match the mixing-layer thickness, shown in Figure 16(b), beyond $\tau > 6$. The logarithmic equation matches the late-time behavior to a similar degree as the power-law, but also exhibits the same trend as the simulation data at earlier times and appears to fit well above $\tau > 0.2$.

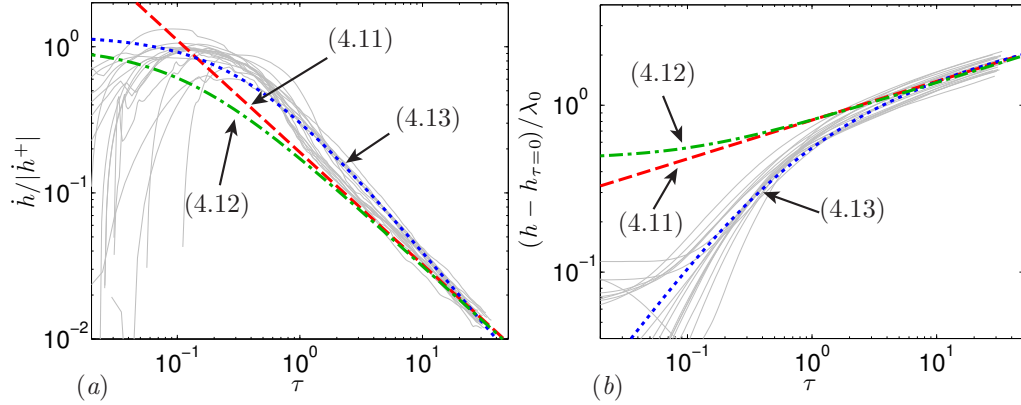


FIGURE 16. Mixing layer (a) growth rate and (b) thickness from all of the cases in Table 1 with curve fits: ----- (red), (4.11); - · - · - (green), (4.12); · · · · · (blue), (4.13).

5. Conclusions

We have derived a model for the initial growth rate of an RMI mixing layer for both light-to-heavy and heavy-to-light cases. The model takes the interfacial perturbations and incident shock Mach number as sole inputs. The model is based on the assumptions that the shock remains planar as it passes through the interface and that the interface is accelerated impulsively. By relating the growth rate of the mixing region to the net mass flux through the equimolar plane, issues of asymmetry, outliers, thresholds etc. are avoided. The model can be applied to any fluid interface, as long as the perturbations are known.

We tested the model against the results of statistically converged three-dimensional large-eddy simulations. The model produces excellent agreement with the simulations for the net mass flux through the equimolar plane immediately after shock passage. This in turn, provides a good estimate of the initial growth rate, which we used, in conjunction with the dominant perturbation wavelength, to scale the growth rates. We found the model to collapse RMI growth rates over the tested range of Atwood numbers ($-0.73 \leq A \leq -0.35$ and $0.35 \leq A \leq 0.73$), Mach numbers ($1.1 \leq M_i \leq 1.9$) and amplitude-to-wavelength ratios ($0.05 \leq \eta_{\text{RMS}}/\lambda_0 \leq 0.4$). For heavy-to-light cases, it is necessary to account for the inversion time of the perturbations. Growth rates arising from different perturbation spectra (Gaussian, power-law, bimodal) collapse reasonably well, although our tests were limited to narrow-band perturbations.

Finally, we examined three curve-fits to the scaled growth rates. The two power-laws fit the mixing-layer thickness beyond a dimensionless time of $\tau > 6$ with an exponent of $\theta = 0.23$. The logarithmic equation appears to provide a better overall fit, exhibiting the same trend as the mixing-layer data beyond $\tau > 0.2$.

Acknowledgements

The authors are grateful to Dr. W. H. Cabot for helpful comments and suggestions regarding this effort. This work was performed under the auspices of the U.S. Department of Energy by Lawrence Livermore National Laboratory under Contract DE-AC52-07NA27344. Additional support was provided to the University of Wisconsin by U.S. DOE Grant No. DE-FG52-06NA26196.

Appendix A. Similarity solution for rarefaction

For the $M_r < 1$ case, the reflected rarefaction is an isentropic similarity flow with solution (Landau & Lifshitz 1987):

$$u_R - u'_1 = \frac{x'_1}{t} + c_R = \frac{2}{\gamma_1 - 1}(c'_1 - c_R) = \frac{2}{\gamma_1 + 1} \left(\frac{x'_1}{t} + c'_1 \right) > 0 ; \quad (\text{A } 1)$$

where x'_1 is the spatial coordinate measured in the frame moving with u'_1 , t is the time since the incident shock hit the interface and u_R and c_R are the lab-frame velocity and sound speed, respectively, inside the rarefaction. In the x'_1 frame, the leading edge of the rarefaction moves to the left with velocity $-c'_1$, the trailing terminus moves either left or right with velocity $u''_1 - u'_1 - c'_1$ and the material interface moves to the right with velocity $u''_1 - u'_1$. The spatial coordinate measured in the lab frame is

$$x = x'_1 + u'_1 t , \quad (\text{A } 2)$$

where $x = x'_1 = 0$ corresponds to the location of the interface at shock impact; hence, the velocity inside the rarefaction is

$$u_R = u'_1 + \frac{2}{\gamma_1 + 1} \left(\frac{x}{t} - u'_1 + c'_1 \right) . \quad (\text{A } 3)$$

This solution is valid in the domain

$$(u'_1 - c'_1)t \leq x \leq (u''_1 - c'_1)t , \quad (\text{A } 4)$$

which is illustrated by the gray region in Figure 3. The thermodynamic state inside the rarefaction is:

$$\rho_R = \rho'_1 \left[1 - \frac{(\gamma_1 - 1)|u_R - u'_1|}{2c'_1} \right]^{2/(\gamma_1 - 1)} , \quad (\text{A } 5)$$

$$p_R = p'_1 \left[1 - \frac{(\gamma_1 - 1)|u_R - u'_1|}{2c'_1} \right]^{2\gamma_1/(\gamma_1 - 1)} , \quad (\text{A } 6)$$

$$c_R = u_R - \frac{x}{t} . \quad (\text{A } 7)$$

Applying the above equations to the terminus of the rarefaction leads to the following relations for the sound speed behind the reflected wave:

$$c'_1 = c'_1 - \frac{\gamma_1 - 1}{2}(u'_2 - u'_1) = c'_1(\Pi_t/\Pi_i)^{(\gamma_1 - 1)/(2\gamma_1)} = (\gamma_1 p'_2/\rho'^2_1)^{1/2} . \quad (\text{A } 8)$$

Appendix B. Post-shock density field for a smooth interface

In order to determine ρ^+ for a diffusive (continuous) interface, consider a differential fluid element with pre-shock and post-shock volumes of dV^- and dV^+ , respectively. If the fluid element is initially located at (x, y, z) then the shock will move it to a new location (x_m, y, z) , where $x_m(x, y, z)$ is a mapping to be determined. We can thus write the post-shock density of the fluid parcel at its new location as

$$\rho^+(x_m, y, z) = \rho^-(x, y, z) \frac{dV^-}{dV^+} . \quad (\text{B } 1)$$

Now let the fluid element be filled with an arbitrary amount of either gas, such that $dV^- = dV_1^- + dV_2^-$, where dV_1^- and dV_2^- are the subvolumes of gases 1 and 2, respec-

tively. The shock compresses these subvolumes such that:

$$dV_1^+ = \frac{\rho_1}{\rho_1''} dV_1^- , \quad (\text{B } 2)$$

$$dV_2^+ = \frac{\rho_2}{\rho_2'} dV_2^- ; \quad (\text{B } 3)$$

hence, the total post-shock volume of the element is

$$dV^+ = dV_1^+ + dV_2^+ = \left[\frac{\rho_1}{\rho_1''} + \left(\frac{\rho_2}{\rho_2'} - \frac{\rho_1}{\rho_1''} \right) \frac{dV_2^-}{dV^-} \right] dV^- . \quad (\text{B } 4)$$

If the gases are initially in hydrostatic equilibrium then the pre-shock volume fraction of gas 2 is

$$\xi^- \equiv \frac{dV_2^-}{dV^-} = \frac{\rho^- - \rho_1}{\rho_2 - \rho_1} ; \quad (\text{B } 5)$$

hence, the post-shock density is

$$\rho^+(x_m, y, z) = \rho^-(x, y, z) \left[\frac{\rho_1}{\rho_1''} + \left(\frac{\rho_2}{\rho_2'} - \frac{\rho_1}{\rho_1''} \right) \xi^-(x, y, z) \right]^{-1} . \quad (\text{B } 6)$$

In order to determine x_m , we write the pre-shock volume as $dV^- = dx dy dz$ and the post-shock volume as $dV^+ = dx_m dy dz$, such that

$$dx_m = \frac{dV^+}{dV^-} dx = \left[\frac{\rho_1}{\rho_1''} + \left(\frac{\rho_2}{\rho_2'} - \frac{\rho_1}{\rho_1''} \right) \xi^-(x, y, z) \right] dx . \quad (\text{B } 7)$$

Integrating (B 7) an arbitrary distance from the perturbed interface yields

$$x_m(x, y, z) = \eta^+(y, z) + \int_{\eta(y, z)}^x \left[\frac{\rho_1}{\rho_1''} + \left(\frac{\rho_2}{\rho_2'} - \frac{\rho_1}{\rho_1''} \right) \xi^-(x^*, y, z) \right] dx^* , \quad (\text{B } 8)$$

where η^+ is given by (3.21). Equation (B 8) provides the location (in terms of x^+) of each density value computed from (B 6).

REFERENCES

- ALON, U., HECHT, J., OFER, D. & SHVARTS, D. 1995 Power laws and similarity of Rayleigh-Taylor and Richtmyer-Meshkov mixing fronts at all density ratios. *Physical review letters* **74** (4), 534–537.
- ASCHENBACH, B., EGGER, R. & TRIMPER, J. 1995 Discovery of explosion fragments outside the vela supernova remnant shock-wave boundary. *Nature* **373**, 587–590.
- BARENBLATT, G. I. 1983 Selfsimilar turbulence propagation from an instantaneous plane source. In *Nonlinear Dynamics and Turbulence* (ed. G. I. Barenblatt, G. Iooss & D. D. Joseph), pp. 48–60. Pitmann.
- BARNES, C. W., BATHA, S. H., DUNNE, A. M., MAGELSEN, G. R., ROTHMAN, S., DAY, R. D., ELLIOTT, N. E., HAYNES, D. A., HOLMES, R. L., SCOTT, J. M., TUBBS, D. L., YOUNGS, D. L., BOEHLY, T. R. & JAANIMAGI, P. 2002 Observation of mix in a compressible plasma in a convergent cylindrical geometry. *Physics of Plasmas* **9** (11), 4431.
- BROUILLETTE, M. 2002 The Richtmyer-Meshkov instability. *Annu. Rev. Fluid Mech.* **34**, 445–468.
- COOK, A. W. 2007 Artificial fluid properties for large-eddy simulation of compressible turbulent mixing. *Phys. Fluids* **19**, 055103.
- COOK, A. W. 2009 Enthalpy diffusion in multicomponent flows. *Phys. Fluids* **21**, 055109.
- COTRELL, D. L. & COOK, A. W. 2007 Scaling the incompressible Richtmyer-Meshkov instability. *Phys. Fluids* **19**, 078105.

- DIMONTE, G. 2000 Spanwise homogeneous buoyancy-drag model for Rayleigh-Taylor mixing and experimental evaluation. *Physics of Plasmas* **7**, 2255–2269.
- DIMONTE, G. & SCHNEIDER, M. 1997 Turbulent Richtmyer–Meshkov instability experiments with strong radiatively driven shocks. *Physics of Plasmas* **4** (12), 4347–4357.
- DIMONTE, G. & SCHNEIDER, M. 2000 Density ratio dependence of Rayleigh-Taylor mixing for sustained and impulsive acceleration histories. *Phys. Fluids* **12**, 304–321.
- GONCHAROV, V. N. 2002 Analytical model of nonlinear, single-mode, classical Rayleigh-Taylor instability at arbitrary atwood numbers. *Physical Review Letters* **88** (13), 134502.
- HECHT, J., ALON, U. & SHVARTS, D. 1994 Potential flow models of Rayleigh-Taylor and Richtmyer-Meshkov bubble fronts. *Physics of Fluids* **6**, 4019–4030.
- HILLEBRANDT, W. & NIEMEYER, J. C. 2000 Type Ia supernova explosion models. *Annual Review of Astronomy and Astrophysics* **38** (1), 191–230.
- JACOBS, J. W. & SHEELEY, J. M. 1996 Experimental study of incompressible Richtmyer-Meshkov instability. *Physics of Fluids* **8** (2), 405–415.
- JUN, B. I., JONES, T. W. & NORMAN, M. L. 1996 Interaction of Rayleigh-Taylor fingers and circumstellar cloudlets in young supernova remnants. *The Astrophysical Journal* **468**, L59–L63.
- LANDAU, L. D. & LIFSHITZ, E. M. 1987 *Fluid Mechanics, Second Edition*. Oxford: Elsevier.
- LAYZER, D. 1955 On the instability of superposed fluids in a gravitational field. *The Astrophysical Journal* **122**, 1–12.
- LEINOV, E., MALAMUD, G., ELBAZ, Y., LEVIN, L. A., BEN-DOR, G., SHVARTS, D. & SADOT, O. 2009 Experimental and numerical investigation of the Richtmyer-Meshkov instability under re-shock conditions. *Journal of Fluid Mechanics* **626**, 449–475.
- LIKHACHEV, O. A. & JACOBS, J. W. 2005 A vortex model for Richtmyer-Meshkov instability accounting for finite atwood number. *Physics of Fluids* **17**, 031704.
- LINDL, J. D., AMENDT, P., BERGER, R. L., GLENDINNING, S. G., GLENZER, S. H., HAAN, S. W., KAUFFMAN, R. L., LANDEN, O. L. & SUTER, L. J. 2004 The physics basis for ignition using indirect-drive targets on the national ignition facility. *Physics of Plasmas* **11** (2), 339.
- MESHKOV, E. E. 1969 Instability of the interface of two gases accelerated by a shock wave. *Izv. Akad. Nauk. SSSR Mekh. Zhidk. Gaza* **4**, 151–157.
- MIKAEILIAN, K. O. 1998 Analytic approach to nonlinear Rayleigh-Taylor and Richtmyer-Meshkov instabilities. *Physical Review Letters* **80** (3), 508–511.
- POINSOT, T. J. & LELE, S. K. 1992 Boundary conditions for direct simulations of compressible viscous flows. *J. Comput. Phys.* **101**, 104–129.
- PRASAD, J. K., RASHEED, A., KUMAR, S. & STURTEVANT, B. 2000 The late-time development of the Richtmyer-Meshkov instability. *Physics of Fluids* **12** (8), 2108–2115.
- RAYLEIGH, LORD 1883 Investigation of the character of the equilibrium of an incompressible heavy fluid of variable density. *Proc. Roy. Math. Soc.* **14**, 170.
- RICHTMYER, R. D. 1960 Taylor instability in shock acceleration of compressible fluids. *Commun. Pure Appl. Math* **23**, 297–319.
- RIKANATI, A., ALON, U. & SHVARTS, D. 1998 Vortex model for the nonlinear evolution of the multimode Richtmyer-Meshkov instability at low atwood numbers. *Physical Review E* **58** (6), 7410–7418.
- TAYLOR, G. I. 1950 The instability of liquid surfaces when accelerated in a direction perpendicular to their plane. *Proc. Roy. Soc. London, Ser. A* **201**, 192.
- THORNER, B., DRIKAKIS, D., YOUNGS, D. L. & WILLIAMS, J. R. 2010 The influence of initial conditions on turbulent mixing due to Richtmyer-Meshkov instability. *J. Fluid Mech.* **654**, 99–139.
- VELIKOVICH, A. L. & DIMONTE, G. 1996 Nonlinear perturbation theory of the incompressible Richtmyer-Meshkov instability. *Physical Review Letters* **76** (17), 3112–3115.
- VETTER, M. & STURTEVANT, B. 1995 Experiments on the Richtmyer-Meshkov instability of an air/SF6 interface. *Shock Waves* **4**, 247–252.
- WRIGHT, J. K. 1961 *Shock Tubes*. London: Methuen.
- YOUNGS, D. L. 1994 Numerical simulation of mixing by Rayleigh-Taylor and Richtmyer-Meshkov instabilities. *Laser and Particle Beams* **12**, 725–750.

- ZHANG, Q. & SOHN, S. I. 1997 Nonlinear theory of unstable fluid mixing driven by shock wave. *Physics of Fluids* **9** (4), 1106–1124.
- ZHANG, Q. & SOHN, S. I. 1996 An analytical nonlinear theory of Richtmyer-Meshkov instability. *Physics Letters A* **212** (3), 149–155.